

# Improved Photoactivity of Pyroxene Silicates by Cation Substitutions

Merid Legesse,<sup>\*,[a]</sup> Heesoo Park,<sup>[a]</sup> Fedwa El Mellouhi,<sup>[a]</sup> Sergey N. Rashkeev,<sup>[a]</sup> Sabre Kais,<sup>[a, b, c]</sup> and Fahhad H. Alharbi<sup>\*,[a, c]</sup>

We investigated the possibility of band structure engineering of pyroxene silicates with chemical formula  $A^{+}B^{3+}Si_2O_6$  by proper cation substitution. Typically, band gaps of naturally formed pyroxene silicates such as  $NaAlSi_2O_6$  are quite high ( $\approx 5$  eV). Therefore, it is important to find a way to reduce band gaps for these materials below 3 eV to make them usable for optoelectronic applications operating at visible light range of the spectrum. Using first-principles calculations, we found that appropriate substitutions of both  $A^{+}$  and  $B^{3+}$  cations can reduce the band gaps of these materials to as low as 1.31 eV.

We also discuss how the band gap in this class of materials is affected by cation radii, electronegativity of constituent elements, spin-orbit coupling, and structural modifications. In particular, the replacement of  $Al^{3+}$  in  $NaAlSi_2O_6$  by another trivalent cation  $Tl^{3+}$  results in the largest band-gap reduction and emergence of intermediate bands. We also found that all considered materials are still thermodynamically stable. This work provides a design approach for new environmentally benign and abundant materials for use in photovoltaics and optoelectronic devices.

## 1. Introduction

Currently, the vast majority ( $\approx 90\%$ ) of solar cell technologies is based on silicon. Recently, significant research efforts have focused on several emerging technologies such as dye-sensitized solar cells<sup>[1–4]</sup> as well as organic<sup>[5–7]</sup> and perovskite photovoltaics.<sup>[8–14]</sup> The main reason for studying these novel materials is to develop cheaper, thinner, and mechanically flexible solar cells in comparison with the conventional silicon based solar cell technologies. However, these technologies face many challenges which should be resolved before large-scale commercialization becomes possible. For example, one of the main concerns with organic-inorganic perovskite solar cells is related to their intrinsic instability.<sup>[9–16]</sup> Therefore, finding alternative materials for solar cells is still an open question. In this work, we explore a new family of light absorbing materials. These materials are abundantly present in the earth crust which guarantees the richness of possible substitutions of their constituent elements as well as their stability and synthesizability.<sup>[17,18]</sup>

The explored materials are the so-called pyroxenes in which silica tetrahedra are the building blocks for corner-sharing network. In one-dimensional systems, they form quasi chains. Pyroxenes are common in meteorites and in extrusive igneous rocks, especially basalt. They form the most abundant group of rock-forming silicates as they were found in almost every igneous rock.<sup>[19–21]</sup> Moreover, it is believed that pyroxenes comprise the majority of components in the Earth's mantle.<sup>[19,20]</sup> Single chain pyroxenes considered in this work have a basic structural unit consisting of linked  $SiO_4$  tetrahedra. Each tetrahedron shares two of its oxygen atoms with adjacent tetrahedrons effectively forming long linear silica chains. Thus the basic structural group is  $Si_2O_6$ , with a Si:O ratio of 1:3. The abundance and variety of pyroxenes as well their phase transition behavior make them interesting materials for a wide range of applications.<sup>[20]</sup> Pyroxenes with a general formula  $ABSi_2O_6$  form an extremely rich class of compounds which are present in the earth's crust.<sup>[22]</sup> In this formula, A and B could be either two divalent cations, or one monovalent and one trivalent cation, respectively. If both A and B are divalent cations (like  $Fe^{2+}$  and  $Mg^{2+}$ ), the resulting structure is orthorhombic, and these materials form the appropriately named orthopyroxene group. At higher temperatures, these structures transform to clinopyroxenitic phase with a monoclinic  $C2/c$  symmetry which undergoes transition to a low temperature clinopyroxenitic phase with  $P2_1/c$  symmetry upon quenching.<sup>[22]</sup>

Among the huge family of pyroxenes, inorganic Na-clinopyroxenes ( $Na^{+}B^{3+}Si_2O_6$ ) has attracted more attention due to their abundance and diversity. Element B may span a huge set of trivalent cations such as: Al, Ga, In, Tl, Sc, Ti, V, Cr, Mn, and Fe, and at room temperature most of them crystallize in a structure with space group  $C2/c$ .<sup>[22–28]</sup> Na-based clinopyroxenes

[a] Dr. M. Legesse, Dr. H. Park, Dr. F. El Mellouhi, Dr. S. N. Rashkeev, Dr. S. Kais, Dr. F. H. Alharbi  
Qatar Environment and Energy Research Institute, Hamad Bin Khalifa University, Doha (Qatar)  
E-mail: MERIDLEGESSE@yahoo.com

[b] Dr. S. Kais  
Department of Chemistry and Physics, Purdue University, West Lafayette, Indiana 46323 (USA)

[c] Dr. S. Kais, Dr. F. H. Alharbi  
College of Science and Engineering, Hamad Bin Khalifa University, Doha (Qatar)  
E-mail: mbelayneh@hbku.edu.qa  
falharbi@hbku.edu.qa

Supporting Information and the ORCID identification number(s) for the author(s) of this article can be found under  
<https://doi.org/10.1002/cphc.201701155>.

are major constituents of many high-pressure rocks (e.g., blueschists, eclogites) and may be involved in chemical reactions (e.g.,  $\text{NaAlSi}_3\text{O}_8 = \text{NaAlSi}_2\text{O}_6 + \text{SiO}_2$ ) which are critically important for understanding the chemistry of the Earth's crust.<sup>[29]</sup> For example, jadeite is a Na-clinopyroxene ( $B = \text{Al}$ ) which is formed under high-pressure conditions (well above 1 GPa); whereas at ambient conditions, the formation of albite ( $\text{NaAlSi}_3\text{O}_8$ ) and nepheline ( $\text{NaAlSi}_3\text{O}_8$ ) is more common.<sup>[27]</sup> The space group of jadeite is monoclinic  $C2/m25$ , and it is composed of silica chains built from  $\text{SiO}_4$  tetrahedra, while the aluminum ions are octahedrally coordinated (see Figure 1).

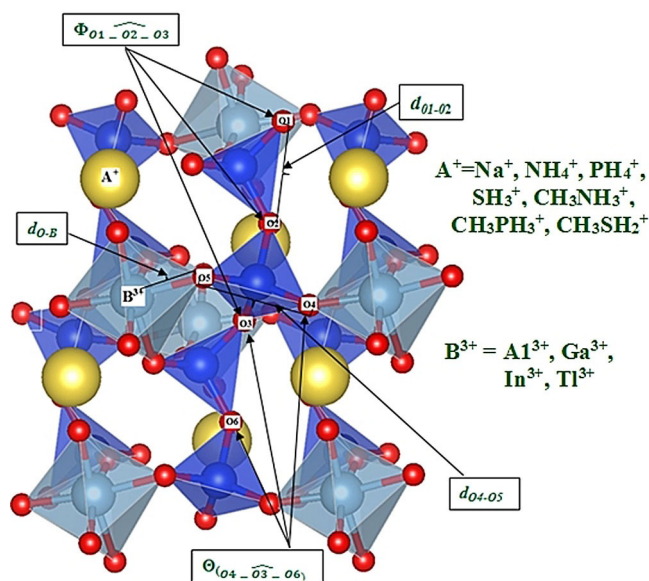


**Figure 1.** Schematic representation of the crystal structure of a  $\text{ABSi}_2\text{O}_6$  pyroxene silicate (A sites are shown as large yellow spheres, B sites as large cyan spheres, Si in blue, O in red).

In this work, we investigate the properties of pyroxene silicates to determine if any of them may be appropriate for optoelectronic and photovoltaic applications. Unfortunately, most of naturally formed inorganic pyroxenes have quite large band gaps ( $\approx 5$  eV). Therefore, they are not suitable for optoelectronic applications operating under visible light conditions.<sup>[29–31]</sup> In order to tune the band gap, we selected different A and B cations in a general  $\text{ABSi}_2\text{O}_6$  pyroxene formula (both atomic and molecular ionic species were used), and for each material constructed in such a way, we performed density functional theory (DFT) based calculations. This methodology allows predicting structural, electronic and optical properties of different inorganic as well as hybrid organic-inorganic pyroxenes. In particular, we found that substituted molecular cations may play a crucial role in modifying the properties of materials. These results are consistent with previous work where molecular cations were found to tune both electronic and optical properties of hybrid perovskites as well as other organic-inorganic frameworks<sup>[13,32,33]</sup> In this work, we report a significant band gap reduction upon molecular cation substitution in pyroxene silicates which makes these materials potentially attractive for optoelectronics and solar cell applications.

## Computational details

We considered two types of substitutions in the  $\text{NaAlSi}_2\text{O}_6$  material: i) replacing  $\text{Na}^+$  cation by a monovalent protonated (containing hydrogen) molecular ion, and; ii) replacing  $\text{Al}^{3+}$  cation B by a Group III metal ion ( $\text{Ga}^{3+}$ ,  $\text{In}^{3+}$ , and  $\text{Tl}^{3+}$ , see Table 1). The candidates for molecular substitution ion for the A site should be monovalent and have a small effective radius to avoid a phase transition in the framework<sup>[32]</sup> which includes:  $\text{NH}_4^+$ ,  $\text{PH}_4^+$ ,  $\text{SH}_3^+$ ,  $\text{CH}_3\text{NH}_3^+$ ,  $\text{CH}_3\text{PH}_3^+$ , and  $\text{CH}_3\text{SH}_2^+$ . The total list of considered materials consists of 28 inorganic and hybrid pyroxenes.

**Table 1.** Calculated primitive vector lengths, angles between them, and total volume of pyroxene unit cells.

Material	Lattice parameters [Å]			Lattice vector angles [°]			Volume [Å <sup>3</sup> ]
	a	b	c	$\alpha$	$\beta$	$\gamma$	
$\text{NaAlSi}_2\text{O}_6$	6.37	6.37	5.22	77.79	102.20	95.30	202.55
$\text{NaGaSi}_2\text{O}_6$	6.48	6.48	5.28	77.86	102.13	95.18	212.28
$\text{NaInSi}_2\text{O}_6$	6.76	6.76	5.35	78.24	101.75	94.58	234.46
$\text{NaTlSi}_2\text{O}_6$	6.85	6.85	5.37	78.72	101.27	94.79	242.19
$\text{NH}_4\text{AlSi}_2\text{O}_6$	6.51	6.51	5.32	77.03	103.06	95.28	214.09
$\text{PH}_4\text{AlSi}_2\text{O}_6$	6.64	6.63	5.58	75.87	104.14	97.43	230.90
$\text{SH}_3\text{AlSi}_2\text{O}_6$	6.59	6.62	5.46	76.75	102.97	95.56	215.04
$\text{CH}_3\text{NH}_3\text{AlSi}_2\text{O}_6$	6.88	7.30	5.62	77.92	114.15	98.45	251.74
$\text{CH}_3\text{PH}_3\text{AlSi}_2\text{O}_6$	6.94	7.55	5.73	78.30	115.05	100.30	265.64
$\text{CH}_3\text{SH}_2\text{AlSi}_2\text{O}_6$	6.91	6.89	5.40	78.79	110.90	94.91	257.09
$\text{NH}_4\text{TlSi}_2\text{O}_6$	7.07	7.12	5.43	98.99	95.28	92.36	267.27
$\text{PH}_4\text{TlSi}_2\text{O}_6$	7.35	7.34	5.56	79.57	101.39	96.66	289.11
$\text{SH}_3\text{TlSi}_2\text{O}_6$	7.36	7.35	5.58	77.28	102.89	100.27	301.80
$\text{CH}_3\text{NH}_3\text{TlSi}_2\text{O}_6$	7.24	7.91	5.62	81.20	107.61	91.80	306.80
$\text{CH}_3\text{PH}_3\text{TlSi}_2\text{O}_6$	8.10	8.15	5.56	84.18	115.47	103.62	338.19
$\text{CH}_3\text{SH}_2\text{TlSi}_2\text{O}_6$	7.94	8.26	5.35	78.79	87.69	94.50	346.92

All calculations were performed using DFT method with Perdew–Burke–Ernzerhof (PBE) density functional<sup>[34]</sup> as implemented in Vienna Ab-initio Simulation Package (VASP).<sup>[35,36]</sup> The electronic wavefunctions were constructed using a plane wave basis set with a cutoff energy of 400 eV. Projector Augmented Wave (PAW) pseudopotentials,<sup>[37,38]</sup> with a [Xe] core for Tl, a [Kr] core for In, [Ar] core for Ga, [Ne] core for Na, Al, Si and S, [He] core for C, O and N, and a one-electron H pseudopotential were used. The Monkhorst–Pack method<sup>[39]</sup> was employed for the Brillouin zone sampling using a  $8 \times 8 \times 8$  k-point mesh; a Gaussian smearing with the width of 0.1 eV was used. The electronic density of states (DOS) was calculated within the Methfessel–Paxton Scheme, and the spin-orbital coupling (SOC) was included in all calculations.

Full structural relaxation of the size and shape of the cell as well as of the atomic positions was conducted with no symmetry constraints until the forces acting on each atom converged to less than  $0.01 \text{ eV}\text{Å}^{-1}$ . For molecular ions, the relaxation procedure started from different initial orientations of the ion. Due to the reduced dimensionality of the considered materials, the Grimmes's semi-empirical van der Waals correction DFT-D2<sup>[40–43]</sup> was included. For the fully relaxed structures, we performed additional  $2 \times 2 \times 2$  k-point single calculations using the HSE06<sup>[44]</sup> hybrid density functional with a 25% parameter for the exact exchange term and a screening length of  $0.2 \text{ Å}^{-1}$ . As known, structure relaxation using PBE density functional is highly accurate.<sup>[33]</sup> The main advantage of using PBE relaxation is that it is considerably more computationally efficient than HSE06 relaxation. For benchmarking, we computed

using HSE06 functional the band gap of  $\text{AlNaSi}_2\text{O}_6$  using both PBE-relaxed and HSE06 relaxed structures and it is found that the difference in band gap is less than 2 meV. However, it is known that PBE functional underestimates the gap<sup>[45]</sup> and hence we use HSE06 functional for optical properties calculation as it is known to be more reliable.<sup>[46–49]</sup> HSE06 gap accuracy is comparable to GW methods.<sup>[50–54]</sup>

The absorption  $\alpha(E)$  and extinction ( $\kappa$ ) coefficients of the designed materials were calculated using the real and imaginary part of the dielectric function [Eq. (1)]:

$$\kappa(E) = \frac{1}{\sqrt{2}} \left( \sqrt{-\epsilon_1 + \sqrt{\epsilon_1^2 + \epsilon_2^2}} \right) \quad (1)$$

and [Eq. (2)]

$$\alpha(E) = \frac{2\pi\kappa(E)}{\lambda(E)} \quad (2)$$

where  $E$  is the photon energy and  $\lambda$  is its wavelength in vacuum.

## 2. Results and Discussion

In this section, we present a detailed analysis of the structural, electronic and optical properties of the pyroxenes. All candidate materials belong to the family of silicates with general formula  $\text{ABSi}_2\text{O}_6$  (where A is a monovalent cation, B is a trivalent cation, Figure 1). We considered only monoclinic crystal structure with the space group  $C2/c$ , which is typical for these materials. First, we calculated the structural and the electronic properties of the materials  $\text{NaBSi}_2\text{O}_6$  where the  $\text{B}^{3+}$  is a trivalent metal ion ( $\text{Al}^{3+}$ ,  $\text{Ga}^{3+}$ ,  $\text{In}^{3+}$ , and  $\text{Tl}^{3+}$ ). Next, for each of the considered B cations, the A (Na) cation is substituted by a protonated molecular cation. Also, we discuss the thermodynamical stability of these materials.

### 2.1. Structural Properties of Inorganic and Hybrid Pyroxenes

The Na-based pyroxenes ( $\text{NaAlSi}_2\text{O}_6$ ,  $\text{NaGaSi}_2\text{O}_6$ , and  $\text{NaInSi}_2\text{O}_6$ ) crystallize in the monoclinic structures according to the data published in the Materials Project database<sup>[55]</sup> and ICSD<sup>[56]</sup>. Crystallographic data were used as an input for the DFT code, then the structures were fully relaxed (Table 1). The optimized lattice parameters for  $\text{NaAlSi}_2\text{O}_6$ ,  $\text{NaGaSi}_2\text{O}_6$ , and  $\text{NaInSi}_2\text{O}_6$  are in good agreement with experimental and theoretical values<sup>[55,57,58]</sup> whereas the structural data of  $\text{NaTlSi}_2\text{O}_6$  has not been reported yet.

Table 1 summarizes the data for optimized pyroxene structures. The ionic radius of the metal ion increases when moving from Al to Tl, resulting in the expansion of the overall volume. This is also accomplished by a slight increase of the lattice parameter  $c$  along the axis parallel to the  $\text{SiO}_4$  chains. A more significant volume increase originates from the increase of  $a$  and  $b$  lattice vectors related to enlarging the size of the edge sharing octahedra centered at the trivalent metal atoms. Further structural analysis of bond lengths and angles between metal cations and oxygen atoms (Table 2) confirms this finding,

**Table 2.** Peroxene structure parameters for the studied materials compared to the parameters of the natural mineral  $\text{NaAlSi}_2\text{O}_6$ : distance between the trivalent metal cation and surrounding oxygen atoms ( $d_{0-B}$ ); distance between two nearest octahedra centred on the B site ( $d_{04-05}$ ); length of the  $\text{SiO}_4$  tetrahedron edge ( $d_{01-02}$ ); and  $\text{SiO}_4$  tetrahedral 1 D chains rotation, bending and distortion angles ( $\Phi$  and  $\Theta$ ).

Structure	Bond length [Å]			Angle [°]	
	$d_{0-B}$	$d_{04-05}$	$d_{01-02}$	$\Phi_{01-02-03}$	$\Theta_{04-03-06}$
$\text{NaAlSi}_2\text{O}_6$	1.85	2.79	2.63	168.8	107.7
$\text{NaGaSi}_2\text{O}_6$	1.93	2.76	2.66	166.7	105.7
$\text{NaInSi}_2\text{O}_6$	2.10	2.71	2.70	163.3	102.7
$\text{NaTlSi}_2\text{O}_6$	2.16	2.69	2.72	161.7	100.9
$\text{NH}_4\text{AlSi}_2\text{O}_6$	1.91	2.83	2.66	173.6	113.1
$\text{PH}_4\text{AlSi}_2\text{O}_6$	1.88	2.79	2.76	167.3	111.5
$\text{SH}_3\text{AlSi}_2\text{O}_6$	1.87	2.73	2.73	178.4	122.4
$\text{CH}_3\text{NH}_3\text{AlSi}_2\text{O}_6$	1.83	2.72	2.84	174.8	117.1
$\text{CH}_3\text{PH}_3\text{AlSi}_2\text{O}_6$	1.93	2.79	2.69	174.8	121.3
$\text{CH}_3\text{SH}_2\text{AlSi}_2\text{O}_6$	1.98	2.89	2.77	171.5	122.0
$\text{NH}_4\text{TlSi}_2\text{O}_6$	2.23	2.77	2.73	168.6	108.2
$\text{PH}_4\text{TlSi}_2\text{O}_6$	2.27	2.84	2.62	172.5	105.2
$\text{SH}_3\text{TlSi}_2\text{O}_6$	2.28	2.85	2.67	155.8	106.9
$\text{CH}_3\text{NH}_3\text{TlSi}_2\text{O}_6$	2.29	2.84	2.65	171.7	115.4
$\text{CH}_3\text{PH}_3\text{TlSi}_2\text{O}_6$	2.10	2.85	2.67	165.6	113.6
$\text{CH}_3\text{SH}_2\text{TlSi}_2\text{O}_6$	2.27	2.81	2.72	159.8	112.3

where  $d_{0-B}$  is distance between the trivalent cation metal and surrounding oxygen atoms and  $d_{04-05}$  is the distance between two nearest octahedra centered at B sites. Structural deviation of the properties of the  $\text{SiO}_4$  chain in the pyroxene structure can be assessed by measuring the distance between  $\text{O}_1$  and  $\text{O}_2$  atoms ( $d_{01-02}$ ) as shown in Figure 1. In addition, the pyroxene  $\text{SiO}_4$  tetrahedral chains experience rotation, bending and distortion (Table 2). The degree of bending is characterized by the deviation of the tetrahedral angle  $\Theta_{04-03-06}$  from the ideal  $109.5^\circ$  and the chain rotation by the deviation of  $\Phi_{01-02-03}$  from the ideal  $180^\circ$ . Both angles confirm the increase of bending and rotation as the size of the metal ion increases in the sequence  $\text{Al} \rightarrow \text{Ga} \rightarrow \text{In} \rightarrow \text{Tl}$ . In terms of bond length, the increased radius of metal ion increases the octahedron size as could be evaluated from the increase of the average  $d_{0-B}$  distance and the slight compression of the interoctahedra distance  $d_{04-05}$ . These effects are partly compensated through a slight elongation of the  $d_{01-02}$  chains along the  $c$  axis characterized by the  $d_{01-02}$  distance. These structural features directly impact the band structure of the material as discussed in the next section.

When  $\text{Na}^+$  in  $\text{NaAlSi}_2\text{O}_6$  is replaced by protonated molecular cations, the cell volume increases due to larger radii of  $\text{NH}_4^+$ ,  $\text{PH}_4^+$  and  $\text{SH}_3^+$  cations compared to  $\text{Na}^+$  (Table 1). The presence of these molecular cations alters considerably both the tetrahedral angle  $\Theta_{04-03-06}$  and the chain rotational angle  $\Phi_{01-02-03}$ . However, it is worth noting that the angular changes depend on the orientation of the molecular cations. Similar to Na-based pyroxenes, the compression of the interoctahedron distance  $d_{04-05}$ , is compensated by an elongation of the chains  $d_{01-02}$  distances along the  $c$  axis. On the contrary,  $d_{0-B}$  decreases when one goes from  $\text{NH}_4^+$  to  $\text{SH}_3^+$  which implies a stronger hydrogen bonding interaction for the nitrogen site  $\text{N-H-O}$  ( $d_{\text{N-H}} = 1.02 \text{ \AA}$  and  $d_{\text{O-H}} = 1.91 \text{ \AA}$  in  $\text{NH}_4\text{TlSi}_2\text{O}_6$ ) than

for the sulfur site S–H–O ( $d_{\text{S-H}}=1.36$  Å and  $d_{\text{O-H}}=1.03$  Å in  $\text{SH}_3\text{TlSi}_2\text{O}_6$ ). This effect is mainly due to the lower electronegativity of S compared to N.

We also performed structural analysis of hybrid peroxenes with  $\text{Na}^+$  substituted by  $\text{CH}_3\text{NH}_3^+$ ,  $\text{CH}_3\text{PH}_3^+$  and  $\text{CH}_3\text{SH}_2^+$  protonated cations. As can be seen from Tables 1 and 2, these molecular cations significantly expand the cell volumes compared to Na-based pyroxenes. The main structural changes are on the  $\Phi_{\text{O1-O2-O3}}$  and  $\Theta_{\text{O4-O3-O6}}$  bond angles, which are larger than those of materials with smaller cations whereas the bond lengths ( $d_{\text{O-B}}$ ,  $d_{\text{O1-O2}}$ , and  $d_{\text{O4-O5}}$ ) do not significantly change.

In Table 1, we have also presented the structural properties of the  $\text{ATlSi}_2\text{O}_6$  compounds. As we already mentioned, the volume of the cell expands with increasing the A-cation radius. The behavior is similar to the  $\text{AAiSi}_2\text{O}_6$  materials. For  $\text{CH}_3\text{PH}_3\text{TlSi}_2\text{O}_6$  and  $\text{CH}_3\text{SH}_2\text{TlSi}_2\text{O}_6$ , unique structural properties were observed. Due to the relatively low electronegativity of P and S, the P–H and S–H bonds are longer than the O–H bonds of the silicate tetrahedra. This aspect was previously reported in the halide perovskites and metavanadates.<sup>[13,14]</sup> In general, substitution of molecular cations in  $\text{ABSi}_2\text{O}_6$  expands the lattice parameters. This is a clear indication that accommodation of large molecular cations in the peroxene structure and related  $\text{SiO}_4$  chain bending and rotation necessarily leads to serious modification of the electronic and optical properties of the materials.

## 2.2. Electronic Properties of Pyroxenes

### 2.2.1. Electronic Structure of $\text{NaAlSi}_2\text{O}_6$ , $\text{NaGaSi}_2\text{O}_6$ , $\text{NaInSi}_2\text{O}_6$ , and $\text{NaTlSi}_2\text{O}_6$ Pyroxenes.

To get an insight into chemical bonding in these materials, we started with B-site substitutions. While any  $\text{BO}_6$  octahedron shares its corners with neighboring  $\text{SiO}_4$  tetrahedrons, we expect that electronic band structure and projected density of states (PDOS) depend on the B-cation radius. Figures 2a–d show band structures and PDOS for some atomic sites in  $\text{NaAlSi}_2\text{O}_6$ ,  $\text{NaGaSi}_2\text{O}_6$ ,  $\text{NaInSi}_2\text{O}_6$ , and  $\text{NaTlSi}_2\text{O}_6$ . It is clear that the conduction band minima (CBM) for all of them are located at the  $\Gamma$  point of the Brillouin zone. On the other hand, the valence band maxima (VBM) are not on any of the high-symmetry points due to the broken symmetry. Thus, the resulted gaps are indirect. For  $\text{NaAlSi}_2\text{O}_6$ , the band gap is 5.32 eV, as follows from PBE+SOC calculations which is consistent with previous theoretical work.<sup>[59]</sup> The VBM is dominated by the O2p orbitals, while the CBM is dominated by O2s and Al3s states.

Substituted Ga, In, and Tl atoms are heavier than Al so relativistic effects are more pronounced for them. Spin-orbit coupling affects the edges of the valence and conduction bands. As observed from Figures 2b–d,  $\text{NaGaSi}_2\text{O}_6$ ,  $\text{NaInSi}_2\text{O}_6$ , and  $\text{NaTlSi}_2\text{O}_6$  compounds are also indirect band gap materials. The VBM is still dominated by the O2p with a minor contribution from 3d, 4d and 5d states of Ga, In, and Tl orbitals, respectively (see Figure 3). On the other hand, the CBM is featured by O2p states hybridized with the 4s, 5s, and 6s states of Ga, In and Tl, respectively. Band structures and PDOSs for  $\text{NaGaSi}_2\text{O}_6$ ,  $\text{NaIn}$

$\text{Si}_2\text{O}_6$ , and  $\text{NaTlSi}_2\text{O}_6$  indicate that “intermediate bands” (isolated narrow bands within the band gap) appear as a consequence of this hybridization. In principle, such intermediate bands can be utilized to increase the efficiency of solar cells beyond that of a single band gap semiconductor.<sup>[51]</sup> Other changes observed at the edge of the valence bands are most likely related to a deformation of  $\text{SiO}_4$  tetrahedral chains instigated by an increase of the B site ionic radius ( $r_{\text{Al}} < r_{\text{Ga}} < r_{\text{In}} < r_{\text{Tl}}$ ).

The calculated band gap values of  $\text{NaAlSi}_2\text{O}_6$ ,  $\text{NaGaSi}_2\text{O}_6$ ,  $\text{NaInSi}_2\text{O}_6$ , and  $\text{NaTlSi}_2\text{O}_6$  materials are summarized in Figure 4. This result suggests that the band gap can be reduced significantly by proper B cation substitution from 5.32 eV (for  $\text{NaAlSi}_2\text{O}_6$ ) to 2.05 eV (for  $\text{NaTlSi}_2\text{O}_6$ ). It is interesting to note that both lattice parameters and the band gaps correlate with the size of valence shell of the B-site cation. When the distance between B cation and O atoms in the  $\text{BO}_6$  octahedron grows (when we move from Al to Tl), one would expect that the overlapping between O2p orbitals and B site s orbitals (Ga 4s, In 5s and Tl 6s) reduces. This should cause a lowering of the CBM which is an antibonding O2p–B s state, that is, the band gap should reduce.

By comparing calculations performed at the PBE and PBE+SOC level, one finds that spin-orbit coupling indeed gives a significant contribution to the reduction of the band gap (by 0.10, 0.21, and 0.32 for  $\text{Ga}^{3+}$ ,  $\text{In}^{3+}$ , and  $\text{Tl}^{3+}$  cations), that is, it should be included. We also compared the calculated gaps using HSE06 hybrid functional to those obtained at the PBE+SOC level. While PBE+SOC calculations underestimate the band gaps as compared to hybrid DFT approach (Figure 4), the correction does not exceed 0.65–0.95 eV for these materials. Therefore, GGA-PBE calculated band gaps could be considered quite reasonable for determining the trends in the band gap modification in pyroxenes.

### 2.2.2. Electronic Structure of Hybrid Organic–Inorganic Pyroxenes

Substitutions of Na at the A site of the  $\text{ABSi}_2\text{O}_6$  compound by protonated molecular cations were also studied, in order to find the dependence of electronic band structure on the effective radius and the dipole moment of the A cation. The analysis is similar to that performed in previous works.<sup>[13,14]</sup> The projected densities of states for  $\text{AAiSi}_2\text{O}_6$  ( $\text{A}=\text{NH}_4^+$ ,  $\text{PH}_4^+$ ,  $\text{SH}_3^+$ ,  $\text{CH}_3\text{NH}_3^+$ ,  $\text{CH}_3\text{PH}_3^+$ , and  $\text{CH}_3\text{SH}_2^+$ ) are shown in Figure 5. The PDOS of  $\text{NH}_4\text{AlSi}_2\text{O}_6$  indicates that H1s and N2p states share electrons, forming a strong covalent N–H bond. Also, the interactions between  $\text{NH}_4^+$  ion with  $\text{Al}^{3+}$  and  $\text{Si}_2\text{O}_6^{4-}$  ions are weak. Due to that,  $\text{NH}_4^+$  cation does not strongly affect the electronic and optical properties of  $\text{NH}_4\text{AlSi}_2\text{O}_6$  as compared to  $\text{NaAlSi}_2\text{O}_6$ . The calculated PDOSs of both  $\text{PH}_4\text{AlSi}_2\text{O}_6$  and  $\text{SH}_3\text{AlSi}_2\text{O}_6$  are shown in Figure 5b,c. Their VBMs are composed mainly of O 2p, with a minor contribution from the 3p and 4p states of  $\text{PH}_4^+$  and  $\text{SH}_3^+$  respectively. The antibonding state related to the interaction between O and  $\text{PH}_4^+$  (or  $\text{SH}_3^+$ ) provides main contribution to the CBM. Due to relatively low electronegativity of P and S (and high electronegativity of O), a nearest O

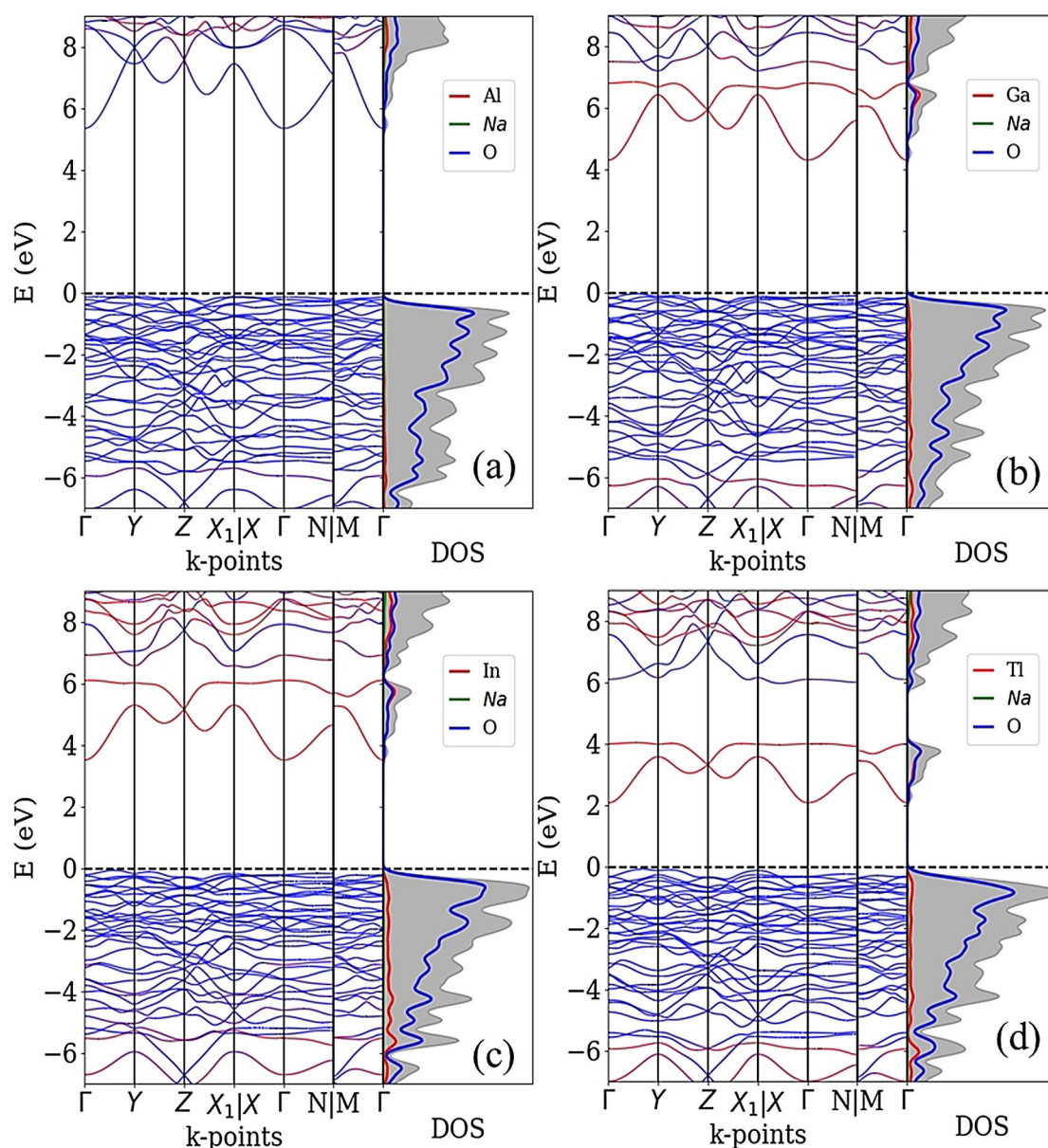


**Figure 2.** Electronic band structure and PDOS for: a)  $\text{NaAlSi}_2\text{O}_6$ ; b)  $\text{NaGaSi}_2\text{O}_6$ ; c)  $\text{NaInSi}_2\text{O}_6$ , and d)  $\text{NaTlSi}_2\text{O}_6$ . The zero energy is positioned at the valence band maximum. All calculations were performed at the PBE + SOC level. The total DOS is indicated by the shadowed area. We did not plot PDOS for Si because its states do not significantly contribute at energies near the band gap.

atom takes some H atoms away from the molecular cation. This results in lowering the conduction band, that is, to the band gap reduction. Nevertheless, the reduced band gaps of  $\text{NH}_4\text{AlSi}_2\text{O}_6$ ,  $\text{PH}_4\text{AlSi}_2\text{O}_6$  and  $\text{SH}_3\text{AlSi}_2\text{O}_6$  still are not sufficiently small to be used in solar cells operating at visible light.

Next, we introduced organic molecular cations  $\text{CH}_3\text{NH}_3^+$ ,  $\text{CH}_3\text{PH}_3^+$ , and  $\text{CH}_3\text{SH}_2^+$ . The presence of the  $\text{CH}_3$  group not only increases the effective ionic radius but also changes the charge distribution around N, P, and S sites. First, it results in an increase of the unit cell volume (Table 1). Additionally, tetrahedral distortion angle ( $\theta_{\text{O}4-\text{O}3-\text{O}6}$ ) increases due to the presence of bigger size molecular cations. These structural changes play significant role in reduction of the band gap. Figures 5 d–f show the PDOSs for  $\text{CH}_3\text{NH}_3\text{AlSi}_2\text{O}_6$ ,  $\text{CH}_3\text{PH}_3\text{AlSi}_2\text{O}_6$ , and

$\text{CH}_3\text{SH}_2\text{AlSi}_2\text{O}_6$  with band gaps of 5.08, 4.81, and 4.36 eV, respectively. All of these band gap values are smaller than those of the materials with  $\text{NH}_4^+$ ,  $\text{PH}_4^+$  and  $\text{SH}_3^+$  molecular cations discussed above. Similar effect is observed for all hybrid pyroxenes with other trivalent cations at the B site ( $\text{Ga}^{3+}$ ,  $\text{In}^{3+}$ , and  $\text{Tl}^{3+}$ )—when  $\text{Na}^+$  is substituted by a protonated molecular cation at the A site, the band gap reduces to lower values than those in the inorganic materials  $\text{NaGaSi}_2\text{O}_6$ ,  $\text{NaInSi}_2\text{O}_6$  and  $\text{NaTlSi}_2\text{O}_6$ .

Focusing on photovoltaic applications, we now examine  $\text{ATiSi}_2\text{O}_6$  as we found that the band gap of  $\text{NaTiSi}_2\text{O}_6$  falls in the range of the visible light. Band structure and PDOS plots of  $\text{ATiSi}_2\text{O}_6$  ( $A = \text{NH}_4^+$ ,  $\text{PH}_4^+$ ,  $\text{SH}_3^+$ ,  $\text{CH}_3\text{NH}_3^+$ ,  $\text{CH}_3\text{PH}_3^+$ ,  $\text{CH}_3\text{SH}_2^+$ ) are shown in Figures 6 a–f. Band structure calculations for all

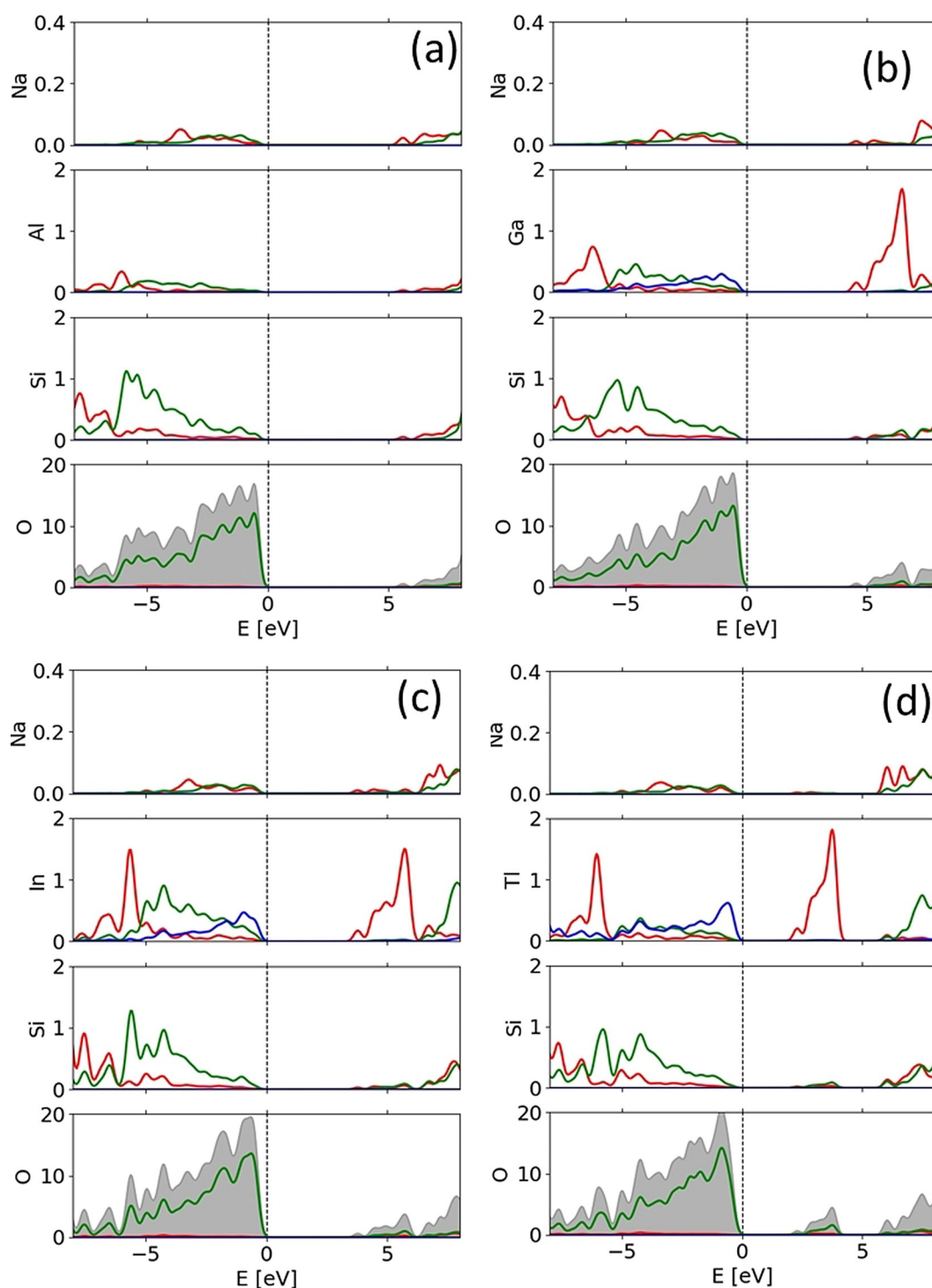


**Figure 3.** PDOS for: a)  $\text{NaAlSi}_2\text{O}_6$ ; b)  $\text{NaGaSi}_2\text{O}_6$ ; c)  $\text{NaInSi}_2\text{O}_6$ , and d)  $\text{NaTlSi}_2\text{O}_6$  pyroxenes (s states are shown in red, p states in green, d states in blue).

Tl based hybrid pyroxenes indicate that both VBM and the CBM are located at the  $\Gamma$  point, so they are direct band gap materials. We performed a detailed study of the PDOSs to study the contribution of different atomic states in the band structure and their possible hybridizations. Unlike  $\text{AAlSi}_2\text{O}_6$  materials, band structures of  $\text{ATlSi}_2\text{O}_6$  clearly indicate the emergence of intermediate bands predominantly related to Tl 6s states with minor contribution from the O 2p states. Figure-

s 6a–c show the band structures and PDOSs of  $\text{NH}_4\text{TlSi}_2\text{O}_6$ ,  $\text{PH}_4\text{TlSi}_2\text{O}_6$ , and  $\text{SH}_3\text{TlSi}_2\text{O}_6$  pyroxenes. When compared to aluminum based  $\text{AAlSi}_2\text{O}_6$  compounds with the same A cations, the band gap values in Tl based materials are significantly smaller due to intermediate bands. Other structural effects include strong alteration of the chain angle  $\Phi_{\text{O}_1-\text{O}_2-\text{O}_3}$ , and strong increase in  $d_{\text{O-B}}$ . In particular, for  $\text{PH}_4$  and  $\text{SH}_3$  materials, 4p and 3p states of S and P hybridize with 2p states of O at

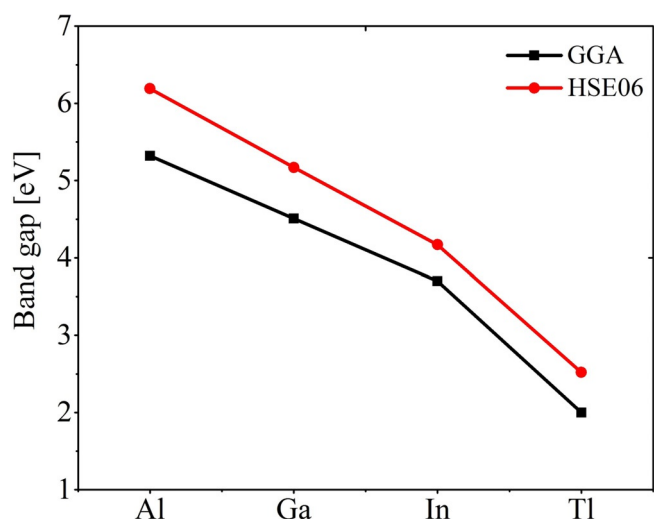


**Figure 4.** Calculated band gaps of  $\text{NaAlSi}_2\text{O}_6$ ,  $\text{NaGaSi}_2\text{O}_6$ ,  $\text{NaInSi}_2\text{O}_6$ , and  $\text{NaTlSi}_2\text{O}_6$  pyroxenes. Calculations conducted at the PBE + SOC level of theory are compared with calculations performed with the hybrid HSE06 density functional.

the VBM. The band structure and PDOS of  $\text{CH}_3\text{NH}_3\text{TlSi}_2\text{O}_6$ ,  $\text{CH}_3\text{PH}_3\text{TlSi}_2\text{O}_6$ , and  $\text{CH}_3\text{SH}_2\text{TlSi}_2\text{O}_6$  are shown in Figures 6d–f. In  $\text{CH}_3\text{NH}_3\text{TlSi}_2\text{O}_6$ , where the hybridization between O2p and Tl6s is weaker than the hybridization between O2p and Al3s in  $\text{CH}_3\text{NH}_3\text{AlSi}_2\text{O}_6$ , the CBM (antibonding state) is pushed downwards and intermediate bands appear.

It is now apparent that by A and B cations substitutions, a significant reduction of band gaps could be achieved (Figure 7). For  $\text{AAAlSi}_2\text{O}_6$  pyroxenes, the band gap of  $\text{CH}_3\text{SH}_2\text{AlSi}_2\text{O}_6$  is 4.36 eV, which is significantly lower than the band gap of inorganic  $\text{NaAlSi}_2\text{O}_6$  pyroxene. In the  $\text{ATlSi}_2\text{O}_6$  pyroxene compounds, the band gap decreases from 2.05 eV (for  $\text{NaTlSi}_2\text{O}_6$ ) to 1.35 eV (for  $\text{CH}_3\text{SH}_2\text{TlSi}_2\text{O}_6$ ). There are many factors responsible for the significant reduction of the band gap including interactions between oxygen and Tl, lattice parameter expansion, spin-orbital coupling, distortion of the tetrahedral angle  $\theta$  and the rotation of chain angle  $\Phi$ . Similar effects were observed for  $\text{AGaSi}_2\text{O}_6$  and  $\text{AlnSi}_2\text{O}_6$  pyroxene compounds as well (see Supporting Information Figures S1, S2).

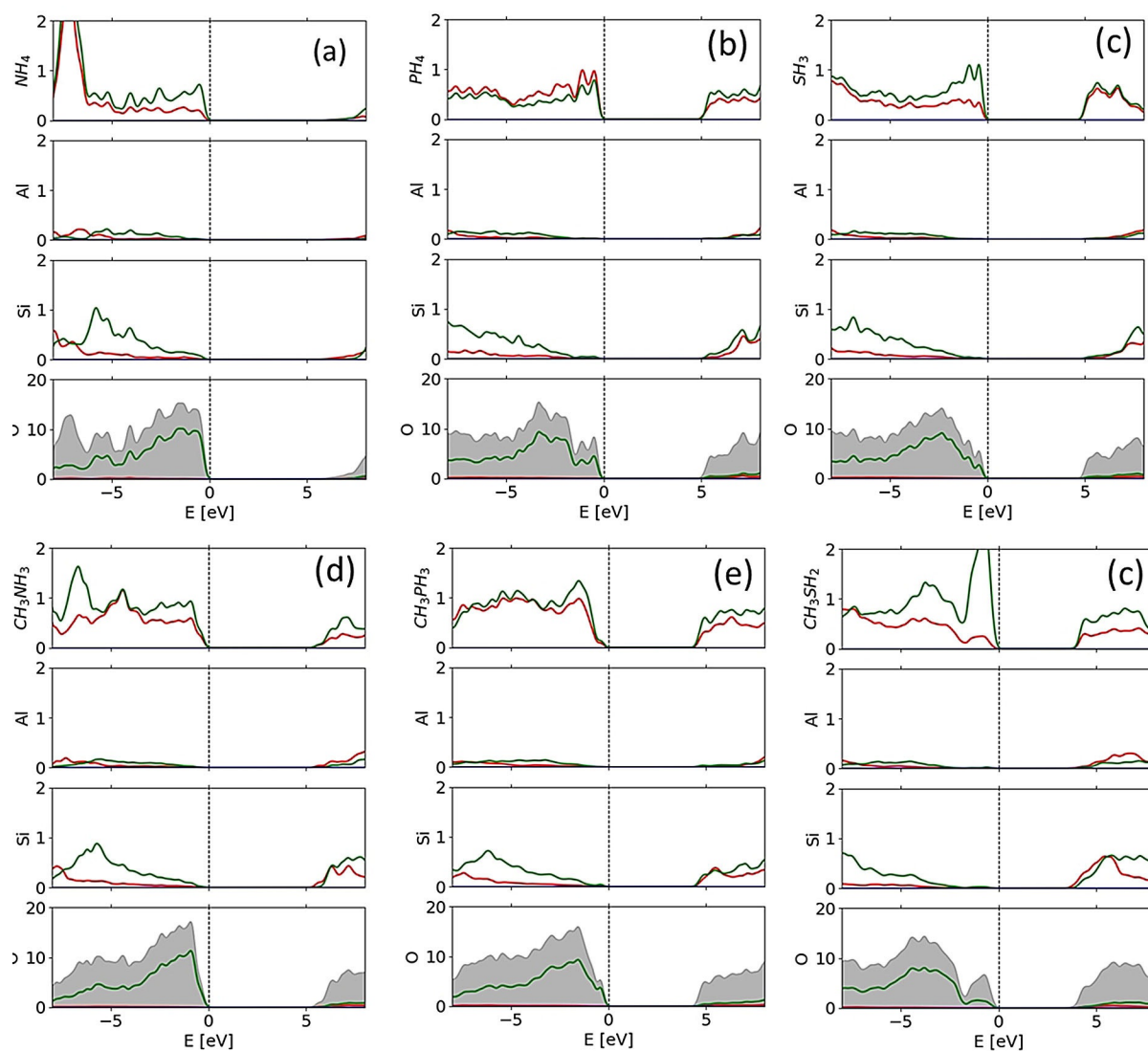


**Figure 5.** PDOS of hybrid  $\text{AAAlSi}_2\text{O}_6$  pyroxene silicates: a)  $\text{NH}_4\text{AlSi}_2\text{O}_6$ ; b)  $\text{PH}_4\text{AlSi}_2\text{O}_6$ ; c)  $\text{SH}_3\text{AlSi}_2\text{O}_6$ ; d)  $\text{CH}_3\text{NH}_3\text{AlSi}_2\text{O}_6$ ; e)  $\text{CH}_3\text{PH}_3\text{AlSi}_2\text{O}_6$ , and f)  $\text{CH}_3\text{SH}_2\text{AlSi}_2\text{O}_6$ . The total DOS is indicated by the shadowed area (s states are shown in red, p states in green, d states in blue).

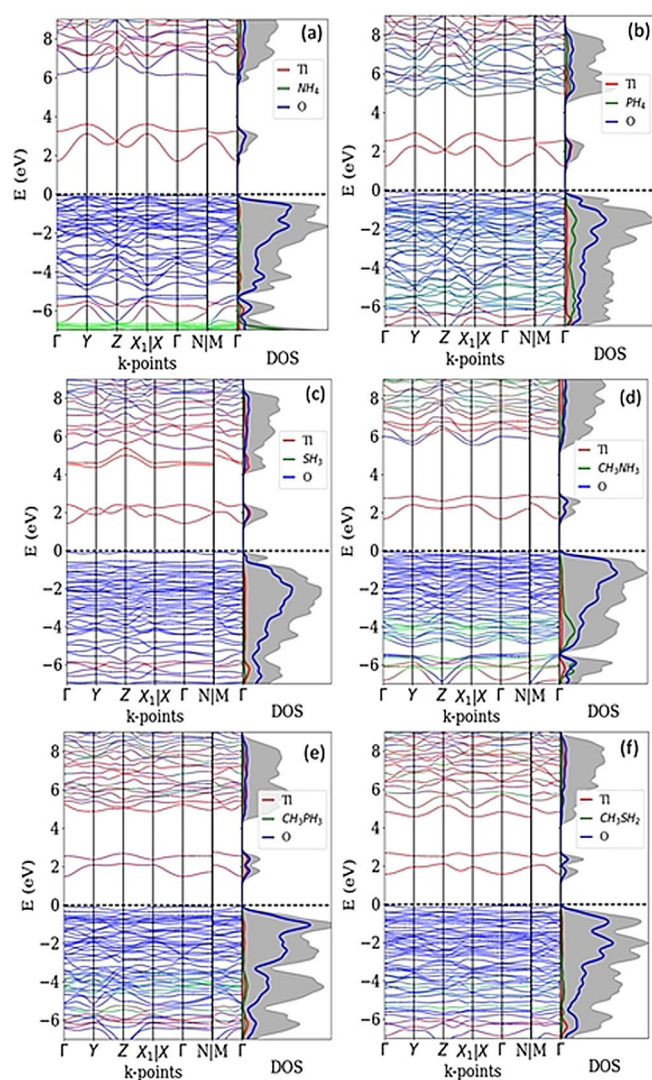


**Figure 6.** Band structure and PDOS of  $\text{ATiSi}_2\text{O}_6$ : a)  $\text{NH}_4\text{TiSi}_2\text{O}_6$ , b)  $\text{PH}_4\text{TiSi}_2\text{O}_6$ , c)  $\text{SH}_3\text{TiSi}_2\text{O}_6$ , d)  $\text{CH}_3\text{NH}_3\text{TiSi}_2\text{O}_6$ , e)  $\text{CH}_3\text{PH}_3\text{TiSi}_2\text{O}_6$ , and f)  $\text{CH}_3\text{SH}_2\text{TiSi}_2\text{O}_6$ . The total density of states (DOS) is indicated by the shadowed area. We did not plot PDOS for silicon because Si states do not significantly contribute at energies near the band gap.

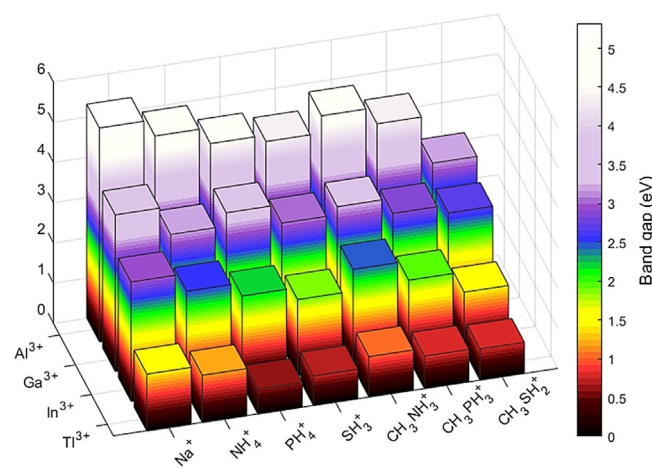


**Figure 7.** Summary of the band-gap values for different atomic and molecular cation substituted pyroxenes.

Hybrid density functional calculations with screened-exchange (HSE06 functional) were performed for  $\text{ATiSi}_2\text{O}_6$  ( $A = \text{NH}_4^+, \text{PH}_4^+, \text{SH}_3^+, \text{CH}_3\text{NH}_3^+, \text{CH}_3\text{PH}_3^+, \text{CH}_3\text{SH}_2^+$ ) to tackle the band gap underestimation problems. The values of the PBE + SOC and HSE06 band gaps of  $\text{ATiSi}_2\text{O}_6$  are shown in Figure 8. The HSE06 values differ from the GGA + SOC results in the range of 0.60–1.1 eV. Interestingly, all HSE06 band gap calculated values for  $\text{ATiSi}_2\text{O}_6$  are still in the visible range. Therefore, these pyroxenes are promising material for optoelectronic applications operating in the visible light conditions.

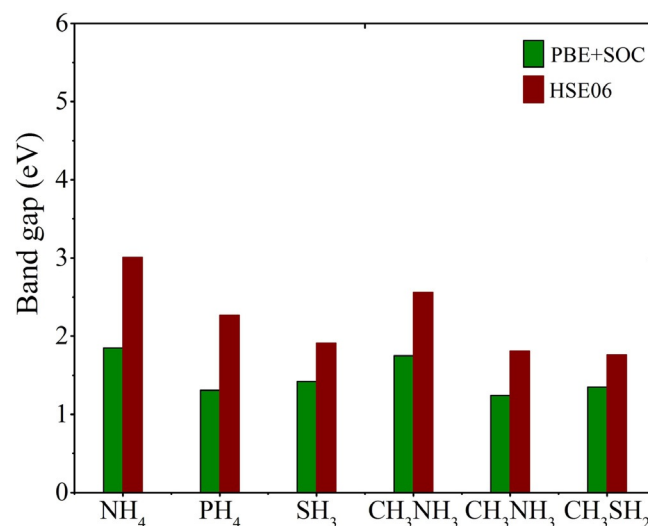


**Figure 8.** Calculated band gaps of  $\text{ATiSi}_2\text{O}_6$  ( $A = \text{NH}_4^+, \text{PH}_4^+, \text{SH}_3^+, \text{CH}_3\text{NH}_3^+, \text{CH}_3\text{PH}_3^+, \text{CH}_3\text{SH}_2^+$ ) using PBE + SOC and the HSE06 hybrid functional (25% HF exchange).

### 2.3. Optical Properties of Hybrid Pyroxenes

We also calculated optical absorption coefficients of pyroxene materials. The imaginary part,  $\epsilon_2$ , of the dielectric function is calculated using band structures and momentum matrix elements, while the real part of the dielectric function,  $\epsilon_1$ , is calculated from  $\epsilon_2$  using the Kramers-Kronig relations.<sup>[58]</sup> The absorption coefficient ( $\alpha$ ) is then calculated directly using both  $\epsilon_1$  and  $\epsilon_2$  [Eq. (2)]. The absorption coefficients of  $\text{NaBSi}_2\text{O}_6$  ( $B = \text{Al}, \text{Ga}, \text{In},$  and  $\text{Tl}$ ) are plotted in Figure 9. As can be observed, the absorption in the lower energy region becomes higher when we go from smaller size cation (Al) to larger size cation (Tl) pyroxenes. Among Na-based pyroxenes,  $\text{NaTiSi}_2\text{O}_6$  has a lowest band gap, and its photoactivity starts at 2.4 eV. Figure 10 shows  $\alpha$  against photon energy for several molecular cations positioned at the A site of the  $\text{AAlSi}_2\text{O}_6$  pyroxenes. The family of  $\text{AAlSi}_2\text{O}_6$  materials has a wider band gap and the absorption starts at 4.55 eV for  $\text{CH}_3\text{SH}_2\text{AlSi}_2\text{O}_6$  and 5.9 eV for  $\text{NH}_4\text{AlSi}_2\text{O}_6$ , which are higher than the visible range.

Finally, we have calculated absorption spectra for  $\text{ATiSi}_2\text{O}_6$  ( $A: \text{NH}_4^+, \text{PH}_4^+, \text{SH}_3^+, \text{CH}_3\text{NH}_3^+, \text{CH}_3\text{PH}_3^+, \text{CH}_3\text{SH}_2^+$ ) (see Figure 11). All these compounds have significant absorption in the visible spectrum due to the low values of their band gaps. The reduction of the band gaps is mainly due to the emergence of intermediate bands.

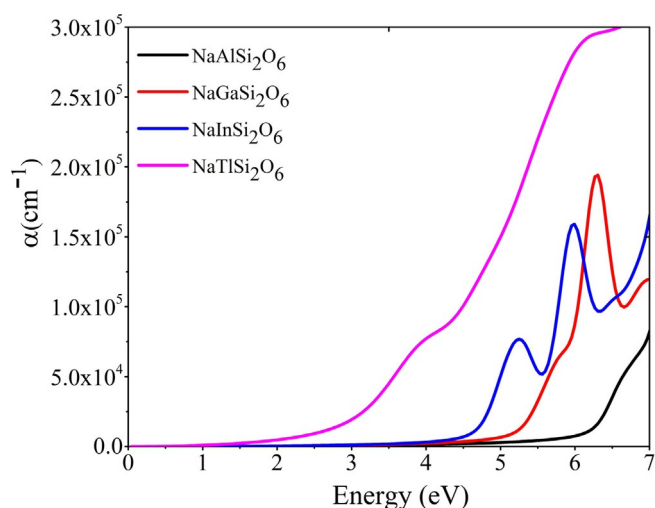


**Figure 9.** Calculated absorption coefficient plotted against energy for  $\text{NaBSi}_2\text{O}_6$  (B: Al, Ga, In, and Tl).

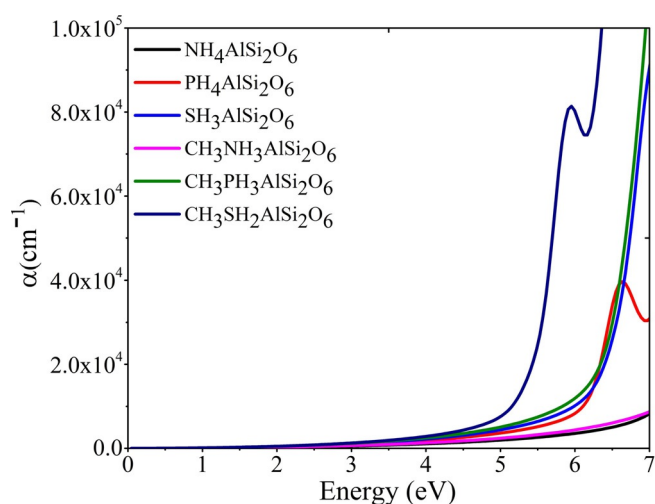


**Figure 10.** Absorption coefficient vs. photon energy for  $\text{AAlSi}_2\text{O}_6$  from HSE06 calculations.

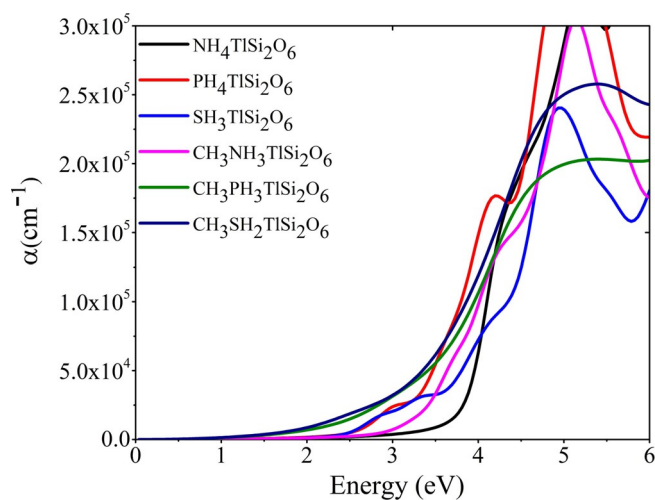


**Figure 11.** Calculated absorption coefficient vs. photon energy for  $\text{ATlSi}_2\text{O}_6$ .

These results indicate that by choosing proper A and B substitution, one can significantly tune the band structure of pyroxene silicates. In particular, organic molecular cation substitutions for the A-site change the band gap within the range of 1 eV, so molecular cations may be used for fine tuning of the band gap.

#### 2.4. Chemical Stability of Hybrid Pyroxenes

The formation energy (energy required to produce a chemical compound from its constituent components) of the system was calculated by using a conventional total energy calculation Scheme. Namely, [Eq. (3)]

$$\Delta E_f = E_{\text{ABSi}_2\text{O}_6} - E_A - E_B - 2E_{\text{Si}} - 3E_{\text{O}_2} \quad (3)$$

where  $\Delta E_f$  is formation energy for the pyroxene compound,  $E_{\text{ABSi}_2\text{O}_6}$ ,  $E_A$ ,  $E_{\text{Si}}$ ,  $E_B$  are total energies for the compound and individual atomic and molecular species which are calculated in the same unit cell. For all the considered materials, the calculated formation energies are negative indicating that they are thermodynamically stable (Figure 12). It should be noted that

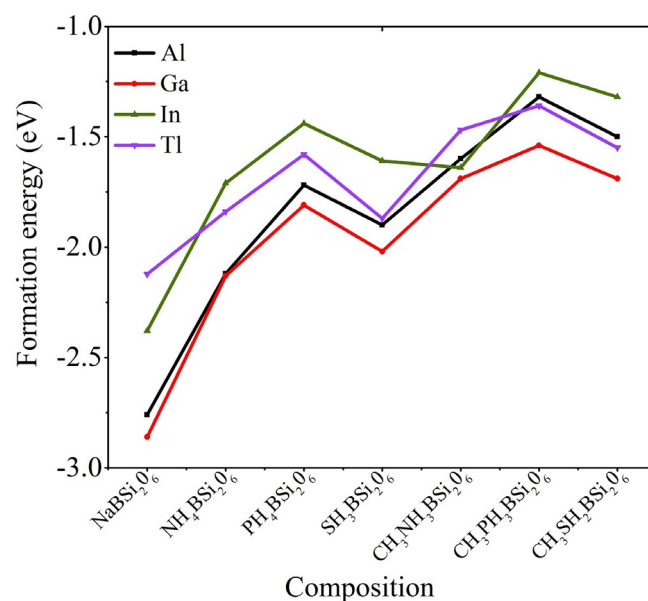


**Figure 12.** Calculated formation energy  $\Delta E_f$  of inorganic and hybrid pyroxene silicates using the (PBE+SOC) theory level.

negative formation energy is a necessary but non-sufficient condition for thermodynamic stability; it just indicates that all  $\text{ABSi}_2\text{O}_6$  structures are formidable; but, there could be other routes for their chemical decomposition. The considered materials become more stable by going in the following order:  $\text{AGaSi}_2\text{O}_6 \rightarrow \text{AAlSi}_2\text{O}_6 \rightarrow \text{ATlSi}_2\text{O}_6 \rightarrow \text{AlnSi}_2\text{O}_6$ . More importantly, the stability of low band gap Tl compounds is comparable to the stability of Al and In compounds that have already been successfully synthesized using a Na cation at the A site.

### 3. Conclusions

DFT calculations have been performed to investigate the structural, electronic, and optical properties as well as thermodynamic stability of hybrid pyroxenes ( $\text{ABSi}_2\text{O}_6$ ) with a variety of configurations. For  $\text{NaBSi}_2\text{O}_6$  pyroxenes, increasing the size of the B cation when going from  $\text{Al}^{3+}$  to  $\text{Ti}^{3+}$  induces the band gap narrowing; so, it is reduced from 5.32 eV in  $\text{NaAlSi}_2\text{O}_6$  to 2.05 eV in  $\text{NaTiSi}_2\text{O}_6$ . Furthermore, we found a substantial band gap reduction and an increase in the optical absorption coefficient upon varying the trivalent metal cation and/or monovalent molecular cation leading to band gaps between 1.0 and 3.0 eV. The calculated formation energies for all the considered pyroxenes are negative indicating that all of them are thermodynamically stable. These results demonstrate the potential of these materials for optoelectronics and solar cell devices.

### Acknowledgements

We would like to thank Qatar National Research Foundation (QNRF) for the support (Grant No. NPRP 7-317-1-055.) Also we would like to thank Texas A&M University at Qatar for computing resources. We would like to thank Ross Hoehn for reading the manuscript prior to submission.

### Conflict of interest

The authors declare no conflict of interest.

**Keywords:** absorption coefficient · band gaps · chemical stability · electronic structure · pyroxene

- [1] A. Hagfeldt, G. Boschloo, L. Sun, L. Kloo, H. Pettersson, *Chem. Rev.* **2010**, *110*, 6595–6663.
- [2] S. Mathew, A. Yella, P. Gao, R. Humphry-Baker, B. F. E. Curchod, N. Ashari-Astani, I. Tavernelli, U. Rothlisberger, M. K. Nazeeruddin, M. Grätzel, *Nat. Chem.* **2014**, *6*, 242–247.
- [3] M. Grätzel, *J. Photochem. Photobiol. C* **2003**, *4*, 145–153.
- [4] M. Law, L. E. Greene, J. C. Johnson, R. Saykally, P. Yang, *Nat. Mater.* **2005**, *4*, 455–459.
- [5] W. Cao, J. Xue, *Energy Environ. Sci.* **2014**, *7*, 2123–2144.
- [6] Y. Yuan, T. J. Reece, P. Sharma, S. Poddar, S. Ducharme, A. Gruverman, Y. Yang, J. Huang, *Nat. Mater.* **2011**, *10*, 296–302.
- [7] L. Lu, M. A. Kelly, W. You, L. Yu, *Nat. Photonics* **2015**, *9*, 491–500.
- [8] W. S. Yang, J. H. Noh, N. J. Jeon, Y. C. Kim, S. Ryu, J. Seo, S. I. Seok, *Science* **2015**, *348*, 1234–1237.
- [9] A. Kojima, K. Teshima, Y. Shirai, T. Miyasaka, *J. Am. Chem. Soc.* **2009**, *131*, 6050–6051.
- [10] J. Luo, J.-H. Im, M. T. Mayer, M. Schreiber, M. K. Nazeeruddin, N.-G. Park, S. D. Tilley, H. J. Fan, M. Grätzel, *Science* **2014**, *345*, 1593–1596.
- [11] C. Motta, F. El-Mellouhi, S. Kais, N. Tabet, F. Alharbi, S. Sanvito, *Nat. Commun.* **2015**, *6*, 7026.
- [12] D. W. de Quilletes, S. M. Vorpahl, S. D. Stranks, H. Nagaoka, G. E. Eperon, M. E. Ziffer, H. J. Snaith, D. S. Ginger, *Science* **2015**, *348*, 683–686.
- [13] F. El-Mellouhi, E. T. Bentría, S. N. Rashkeev, S. Kais, F. H. Alharbi, *Sci. Rep.* **2016**, *6*, 30305.
- [14] F. El-Mellouhi, A. Marzouk, E. T. Bentría, S. N. Rashkeev, S. Kais, F. H. Alharbi, *ChemSusChem* **2016**, *9*, 2648–2655.
- [15] S. De Wolf, J. Holovsky, S.-J. Moon, P. Löper, B. Niesen, M. Ledinsky, F.-J. Haug, J.-H. Yum, C. Ballif, *J. Phys. Chem. Lett.* **2014**, *5*, 1035–1039.
- [16] D. Wang, M. Wright, N. K. Elumalai, A. Uddin, *Sol. Energy Mater. Sol. Cells* **2016**, *147*, 255–275.
- [17] F. Alharbi, J. D. Bass, A. Salhi, A. Alyamani, H.-C. Kim, R. D. Miller, *Renewable Energy* **2011**, *36*, 2753–2758.
- [18] T. Kalil, C. Wadia, Committee on Technology National Science and Technology Council, **2011**.
- [19] W. A. Deer, R. A. Howie, J. Zussman in *Rock-forming Minerals: Feldspars*, Volume 4A, Geological Society of London, London, **2001**.
- [20] W. A. Deer, R. A. Howie, J. Zussman, *An introduction to the rock-forming minerals*, Longman Scientific & Technical, Hong Kong, **1992**.
- [21] A. E. Ringwood, *Geochim. Cosmochim. Acta* **1991**, *55*, 2083–2110.
- [22] J. S. Monroe, R. Wicander, *The changing earth: exploring geology and evolution*, Cengage Learning, **2011**.
- [23] S. V. Streltsov, D. I. Khomskii, *Phys. Rev. B* **2008**, *77*, 064405.
- [24] S. Jodlauk, P. Becker, J. A. Mydosh, D. I. Khomskii, T. Lorenz, S. V. Streltsov, D. C. Hezel, L. Bohatý, *J. Phys. Condens. Matter* **2007**, *19*, 432201.
- [25] A. M. Walker, *Phys. Earth Planet. Inter.* **2012**, *192*, 81–89.
- [26] C. T. Prewitt, C. W. Burnham, *Am. Mineral.* **1966**, *51*, 956–975.
- [27] M. Cameron, S. Sueno, C. T. Prewitt, J. J. Papike, *Am. Mineral.* **1973**, *58*, 594–618.
- [28] J. R. Clarke, D. E. Appleman, J. J. Papike, *Mineral. Soc. Am. Spec. Pap.* **1969**, *31*, 2–4.
- [29] S. D. Jackson, J. S. J. Hargreaves, *Metal oxide catalysis*, Wiley-VCH, Weinheim, **2008**.
- [30] M. I. Hossain, F. H. Alharbi, *Mater. Technol.: Adv. Perform. Mater.* **2013**, *28*, 88–97.
- [31] Y. Murakami, E. Einarsson, T. Edamura, S. Maruyama, *Phys. Rev. Lett.* **2005**, *94*, 087402.
- [32] A. A. B. Baloch, S. P. Aly, M. I. Hossain, F. El-Mellouhi, N. Tabet, F. H. Alharbi, *Sci. Rep.* **2017**, *7*, 11984.
- [33] F. El-Mellouhi, A. Akande, C. Motta, S. N. Rashkeev, G. Berdiyev, M. E. A. Madjet, A. Marzouk, E. T. Bentría, S. Sanvito, S. Kais, *ChemSusChem* **2017**, *10*, 1931–1942.
- [34] J. P. Perdew, J. A. Chevary, S. H. Vosko, K. A. Jackson, M. R. Pederson, D. J. Singh, C. Fiolhais, *Phys. Rev. B* **1992**, *46*, 6671.
- [35] G. Kresse, J. Hafner, *Phys. Rev. B* **1993**, *47*, 558.
- [36] G. Kresse, J. Furthmüller, *Phys. Rev. B* **1996**, *54*, 11169.
- [37] P. E. Blöchl, *Phys. Rev. B* **1994**, *50*, 17953.
- [38] G. Kresse, D. Joubert, *Phys. Rev. B* **1999**, *59*, 1758.
- [39] H. J. Monkhorst, J. D. Pack, *Phys. Rev. B* **1976**, *13*, 5188.
- [40] H. Rydberg, M. Dion, N. Jacobson, E. Schröder, P. Hyldgaard, S. I. Simak, D. C. Langreth, B. I. Lundqvist, *Phys. Rev. Lett.* **2003**, *91*, 126402.
- [41] M. Dion, H. Rydberg, E. Schröder, D. C. Langreth, B. I. Lundqvist, *Phys. Rev. Lett.* **2004**, *92*, 246401.
- [42] D. C. Langreth, M. Dion, H. Rydberg, E. Schröder, P. Hyldgaard, B. I. Lundqvist, *Int. J. Quantum Chem.* **2005**, *101*, 599–610.
- [43] K. Lee, É. D. Murray, L. Kong, B. I. Lundqvist, D. C. Langreth, *Phys. Rev. B* **2010**, *82*, 081101.
- [44] J. Heyd, G. E. Scuseria, M. Ernzerhof, *J. Chem. Phys.* **2003**, *118*, 8207–8215.
- [45] J. P. Perdew, *Int. J. Quantum Chem.* **1985**, *28*, 497–523.
- [46] M. Legesse, M. Nolan, G. Fagas, *J. Phys. Chem. C* **2013**, *117*, 23956–23963.
- [47] M. L. Belayneh, *First principles simulation of amorphous silicon bulk, interfaces, and nanowires for photovoltaics*, PhD Thesis, University College Cork **2015**.
- [48] A. J. Garza, G. E. Scuseria, *J. Phys. Chem. Lett.* **2016**, *7*, 4165–4170.
- [49] M. Jain, J. R. Chelikowsky, S. G. Louie, *Phys. Rev. Lett.* **2011**, *107*, 216806.
- [50] J. M. Crowley, J. Tahir-Kheli, W. A. Goddard III, *J. Phys. Chem. Lett.* **2016**, *7*, 1198–1203.
- [51] L. Chiodo, J. M. García-Lastra, A. Iacomino, S. Ossicini, J. Zhao, H. Petek, A. Rubio, *Phys. Rev. B* **2010**, *82*, 045207.
- [52] E. Mosconi, P. Umari, F. De Angelis, *Phys. Chem. Chem. Phys.* **2016**, *18*, 27158–27164.
- [53] S. Z. Karazhanov, P. Ravindran, A. Kjekshus, H. Fjellvåg, B. G. Svensson, *Phys. Rev. B* **2007**, *75*, 155104.
- [54] J.-W. Park, S. H. Eom, H. Lee, J. L. F. Da Silva, Y.-S. Kang, T.-Y. Lee, Y. H. Khang, *Phys. Rev. B* **2009**, *80*, 115209.
- [55] K. Persson in *Materials Data on NaAl (SiO<sub>3</sub>)<sub>2</sub> (SG: 15) by Materials Project, LBNL Materials Project*; Lawrence Berkeley National Laboratory (LBNL), Berkeley, CA (United States), City, **2014**.

- [56] G. Bergerhoff, R. Hundt, R. Sievers, I. D. Brown, *J. Chem. Inf. Comput. Sci.* **1983**, *23*, 66–69.
- [57] J. Yang, L. Yang, J. Long, *Mater. Sci. Semicon. Pro.* **2015**, *31*, 509–516.
- [58] H. S. Bennett, E. A. Stern, *Phys. Rev.* **1965**, *137*, A448.

- [59] F. H. Alharbi, S. Kais, *Renewable Sustainable Energy Rev.* **2015**, *43*, 1073–1089.

---

Manuscript received: October 24, 2017

Revised manuscript received: December 7, 2017

Accepted manuscript online: January 4, 2018

Version of record online: February 23, 2018

---